crystals

MDPI

Article

Exploring Brannerite-Type $Mg_{1-x}M_xV_2O_6$ (M = Mn, Cu, Co, or Ni) Oxides: Crystal Structure and Optical Properties

Hua-Chien Hsu [1], Narayanan Lakshminarasimhan [1,2], Jun Li [1], Arthur P. Ramirez [3] and Mas A. Subramanian [1,*]

[1] Department of Chemistry, Oregon State University, Corvallis, OR 97331, USA; hsuh@oregonstate.edu (H.-C.H.); laksnarasimhan@cecri.res.in (N.L.); jun.li@oregonstate.edu (J.L.)
[2] CSIR-Central Electrochemical Research Institute, Karaikudi 630003, Tamil Nadu, India
[3] Department of Physics, University of California Santa Cruz, Santa Cruz, CA 95064, USA; apr@ucsc.edu
* Correspondence: mas.subramanian@oregonstate.edu

Abstract: Environmentally benign, highly stable oxides exhibiting desirable optical properties and high near-IR reflectance are being researched for their potential application as pigments. $Mg_{1-x}M_xV_2O_6$ (M = Mn, Cu, Co, or Ni) oxides with brannerite-type structures were synthesized by the conventional solid-state reaction method to study their optical properties. These series exhibit structural transitions from brannerite ($C2/m$) to distorted brannerite ($P\bar{1}$) and NiV_2O_6-type ($P\bar{1}$) structures. The average color of $Mg_{1-x}M_xV_2O_6$ compounds varies from reddish-yellow to brown to dark brown. The $L^*a^*b^*$ color coordinates reveal that $Mg_{1-x}Cu_xV_2O_6$ and $Mg_{1-x}Ni_xV_2O_6$ show more red hues in color with x = 0.4 and x = 0.5, respectively. The UV–Vis diffuse reflectance spectra indicate a possible origin for these results include the ligand-to-metal charge transfer (O^{2-} 2p-V^{5+} 3d), metal-to-metal charge transfer (from Mn^{2+} 3d/Cu^{2+} 3d/Co^{2+} 3d/Ni^{2+} 3d to V^{5+} 3d), band gap transitions, and d–d transitions. Magnetic property measurements revealed antiferromagnetic behavior for the compounds $Mg_{1-x}M_xV_2O_6$ (M = Mn, Cu, Co, and Ni), and an oxidation state of +2 for the M ions was deduced from their Curie–Weiss behavior. The system $Mg_{1-x}Mn_xV_2O_6$ has a NIR reflectance in the range between 40% and 70%, indicating its potential to be utilized in the pigment industry.

Keywords: optical properties; magnetic properties; transition metal oxides

Academic Editor: Yulia V. Nelyubina

Received: 29 December 2024
Revised: 9 January 2025
Accepted: 13 January 2025
Published: 16 January 2025

Citation: Hsu, H.-C.; Lakshminarasimhan, N.; Li, J.; Ramirez, A.P.; Subramanian, M.A. Exploring Brannerite-Type $Mg_{1-x}M_xV_2O_6$ (M = Mn, Cu, Co, or Ni) Oxides: Crystal Structure and Optical Properties. *Crystals* **2025**, *15*, 86. https://doi.org/10.3390/cryst15010086

1. Introduction

Transition metal oxides have attracted significant attention in the field of solid-state chemistry since the discovery of their various captivating colors, such as chrome green (Cr_2O_3) and cobalt blue ($CoAl_2O_4$), which are the currently used commercial inorganic pigments. However, there are concerns about Cr and Co due to their high toxicity to the environment and/or durability among commercial pigments [1–3]. The objective of the present study is to explore environmentally friendly, intense, durable, and cost-effective inorganic colorants for the pigment industry. Vanadium, a 3d transition metal, exhibits various oxidation states, +3, +4, and +5, in oxides such as V_2O_3, VO_2, and V_2O_5. Due to these oxidation states, vanadium oxides exhibit a diverse range of useful properties such as magnetic, catalytic, electrochemical energy storage in lithium-ion batteries, and optical properties [4–6]. The optical absorption of vanadium oxides lies in the near-UV-to-visible region, where ligand-to-metal charge transfer (LMCT) electronic transitions from O^{-2} 2p to V^{+5} 3d occur.

The serendipitous discovery of the intense blue pigment Y(In,Mn)O_3 highlighted new directions for tuning pigments through structural–substitutional rationales, enabling structures amenable to substituting various transition metal ions to have their optical properties tuned accordingly [1]. For example, brannerite is a brown-colored uranium titanate mineral (UTi_2O_6), and the composition of this structure can differ extensively [7]. The general formula can be described as AB_2O_6, and this structure has larger *A* cations with divalent metal and small-sized *B* ions [8]. The structure of brannerite (AB_2O_6) is monoclinic with the space group $C2/m$ in which *A* and *B* sites are octahedrally coordinated, forming chains of edge-sharing AO_6 connected to edge-sharing BO_6 octahedral units (Figure 1). The distance of *A*–*A* within the chains is 3.53 Å, and the angle of ∠*A*–O–*A* is 104.7°; the *A*–*A* distance between chains is 4.97 Å [9]. The divalent metal vanadium oxides, MV_2O_6 (*M* = Mg, Ca, Mn, Co, Ni, Cu, and Zn), have been widely studied for their magnetic, photocatalytic, fuel cell, battery applications, etc. [10–12]. Even as an inorganic–organic hybrid, the observed one-dimensional ferromagnetic interactions above the Néel temperature in the antiferromagnetic brannerite-type $[\{Mn(Bpy)_x\}(VO_3)_2] \approx (H_2O)_y$ [x = 0.5 or 1; y = 0.62 or 1.12] reveals the potential of brannerites as quantum materials [13]. Furthermore, solid solution systems can be realized in the brannerite types like MnV_2O_6–MoO_3, MgV_2O_6–CaV_2O_6, ZnV_2O_6–CaV_2O_6, and MnV_2O_6–CaV_2O_6 [9,14–16]. Lakshminarasimhan et al. recently reported the structure–optical property relationships of the solid solution $Ca_{1-x}Mn_xV_2O_6$ and $Zn_{1-x}Co_xV_2O_6$ [17]. We also note that MgV_2O_6 exhibits a higher reflectance in the near-infrared (NIR) region compared to other divalent metal vanadium oxides. Therefore, MgV_2O_6, when combined with transition metals, could potentially exhibit strong reflectance in the NIR region, making these materials effective in energy-saving applications on rooftops and vehicles [2,3].

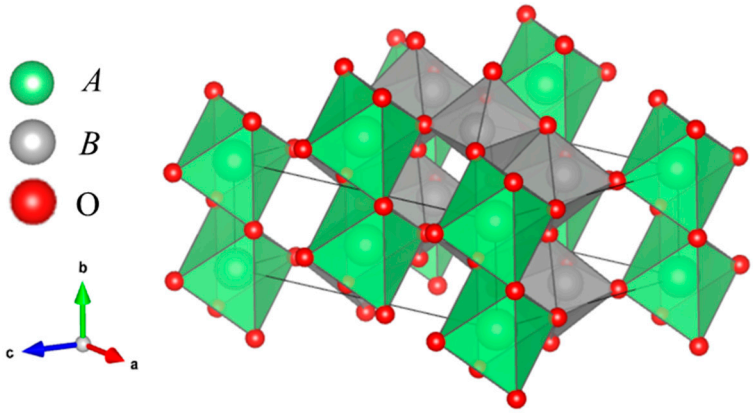

Figure 1. The unit cell of an ideal brannerite structure with the space group, $C2/m$. The general formula is AB_2O_6. The *A* and *B* sites are octahedrally coordinated, forming chains of edge-sharing AO_6 connected to edge-sharing BO_6.

It is not surprising that not all MV_2O_6 compounds have this ideal brannerite-type structure, as variations in the structure can be expected due to differences in stoichiometry. For example, CuV_2O_6 is a slight distortion of the brannerite structure with the space group $P\bar{1}$ and consists of CuO_6 and VO_6 groups (Figure 2a). The Cu–Cu distance along the b-axis is 3.54 Å, and the ∠Cu–O–Cu bond angle is 103.99° within the chains, whereas the Cu–Cu distance along the a-axis is 4.97 Å between the chains [18]. α-CuV_2O_6 shows quasi-one-dimensional behavior with short-range magnetic ordering and on cooling towards a long-range antiferromagnetic transition at 24 K [19,20]. On the other hand, MV_2O_6 (*M* = Co and Ni) have NiV_2O_6-type structures with the space group ($P\bar{1}$) formed by MO_6 and corner-shared VO_4 and corner- and edge-shared VO_6 (Figure 2b). The *M*–*M* distance along the b-axis is 2.96 Å, and the ∠*M*–O–*M* bond angle is 92.67° within the chains,

whereas the *M*–*M* distance along the a-axis is 7.13 Å between the chains in the NiV_2O_6-type structure [21]. Comparing these three brannerite-related structures, we have the ideal brannerite with a monoclinic angle greater than 110°, the distorted brannerite with a triclinic angle around 110°, and the NiV_2O_6-type with a triclinic angle approximately 93°. The structures of these compounds show octahedral coordination of the *M*-site ion by oxygen, often with distortion attributable to the varying magnitudes of the Jahn–Teller effect exhibited by each metal ion [22].

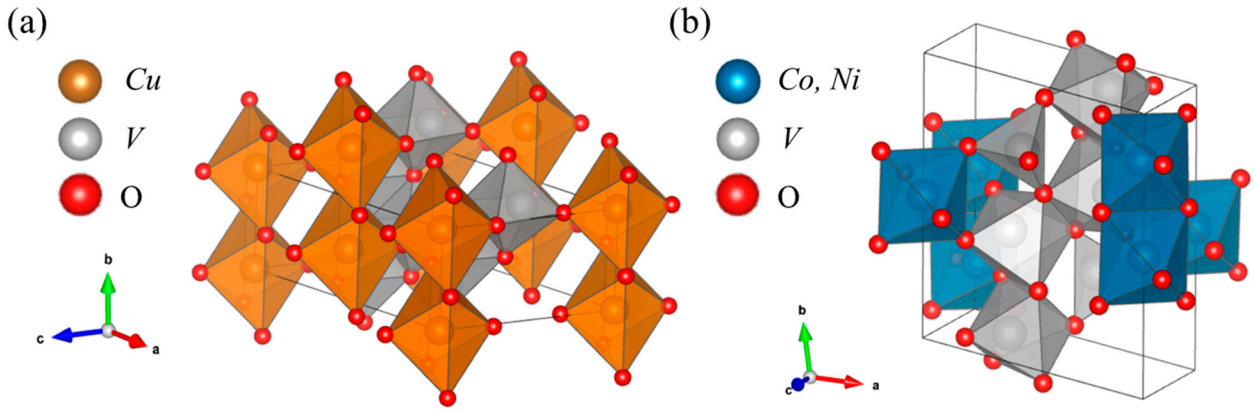

Figure 2. (**a**) The unit cell of a slightly distorted brannerite structure (CuV_2O_6) with the space group, $P\bar{1}$. (**b**) The unit cell of NiV_2O_6-type structures with the space group, $P\bar{1}$, formed by MO_6 (*M* = Co or Ni) and corner-shared VO_4 and corner- and edge-shared VO_6.

The valence states of transition metal ions and the crystal structure of the series played vital roles in the origin of the color of the samples reported here [2]. To further explore the optical properties of brannerite-type oxides, here, we report a new series $Mg_{1-x}M_xV_2O_6$ (*M* = Mn, Cu, Co, or Ni; *x* = 0.0 to 1.0) and their optical properties. The structures in the solid solution are also further investigated through powder X-ray diffraction (XRD), with refinements of the lattice parameters. The structure–optical property relationships are shown for the series $Mg_{1-x}M_xV_2O_6$ (*M* = Mn, Cu, Co, or Ni).

2. Experimental

2.1. Synthesis

We synthesized $Mg_{1-x}M_xV_2O_6$ (*M* = Mn, Cu, Co, or Ni) compounds, with *x* ranging from 0.0 to 1.0, using the conventional high-temperature solid-state reaction method. Stoichiometric amounts of MgO (Alfa Aesar, Ward Hill, MA, USA, 99.5%), $MnCO_3$ (Alfa Aesar, Ward Hill, MA, USA, 99.9%), $Co(OH)_2$ (Alfa Aesar, Ward Hill, MA, USA, 97%), CuO (Fluka, Buchs, Switzerland, 99.9%), NiO (Alfa Aesar, Ward Hill, MA, USA, 99.99%), and V_2O_5 (Johnson Matthey, London, United Kingdom, 99.9%) were ground thoroughly using an agate mortar and pestle. After the mixture was homogeneous and fine, the starting materials were pressed into pellets with an applied pressure of 0.8 psi and transferred into an alumina ceramic crucible and heated in air between 600 and 700 °C for 12 h in a muffle furnace. The solid solutions $Mg_{1-x}Cu_xV_2O_6$ and $Mg_{1-x}Mn_xV_2O_6$ series were sintered at least twice at 600 °C and 700 °C with intermediate grinding, respectively, while the synthesis temperature of $Mg_{1-x}Co_xV_2O_6$ and $Mg_{1-x}Ni_xV_2O_6$ was 650 °C with repeated heating at least twice.

2.2. Characterization

Phase formation was confirmed through powder X-ray diffraction (XRD) using a Rigaku Miniflex II X-ray Diffractometer (Rigaku, Tokyo, Japan) with Cu-Kα radiation.

The lattice parameters were obtained by Le Bail fitting using GSAS/EXPGUI software First version [23,24]. An internal standard, NaCl ($Fm\bar{3}m$; Sigma Aldrich, St. Louis, MO, USA, 99.99%), was used while recording the XRD. Crystal structures were generated using VESTA 3.5.8 software [25]. Diffuse reflectance UV–Vis (DRUV–Vis) and NIR reflectance spectra (up to 2500 nm) were obtained using a Jasco V-670/V-770 spectrophotometer (JASCO, Tokyo, Japan). The data were converted to absorbance using the Kubelka–Munk equation. The $L^*a^*b^*$ color coordinates were measured using a Konica Minolta CM-700d spectrophotometer (Konica Minolta, Tokyo, Japan). The magnetization measurements were performed using a commercial magnetometer (MPMS3, Quantum Design, San Diego, CA, USA) in the temperature range 5–350 K.

3. Results and Discussion

3.1. Structural Analysis

The phase formation of $Mg_{1-x}M_xV_2O_6$ (M = Mn, Cu, Co, or Ni; x = 0.0–1.0) was analyzed by powder XRD. Figure S1, in the Supporting Information, shows the powder XRD patterns of solid-solution $Mg_{1-x}Mn_xV_2O_6$ prepared at 700 °C in air. The end members, despite having the same space group ($C2/m$), the solid solution exhibited a mixture of phases, resulting in a miscibility gap (x = 0.4–0.8) due to slight variations in the unit cell edges for the end members. The lattice parameters of the samples were refined in order to further investigate the structures by Le Bail fitting. The lattice parameters and unit cell volume vs. x in the $Mg_{1-x}Mn_xV_2O_6$ are shown in Figure S2. The lattice parameters and unit cell volume increase upon Mn substitution due to the larger ionic radii of Mn^{2+} (0.83 Å) when compared to Mg^{2+} (0.72 Å) in six coordination [26].

Similarly, $Mg_{1-x}Cu_xV_2O_6$ (x = 0.0–1.0) samples were synthesized at 600 °C in air, and the powder XRD patterns are shown in Figure 3. The $Mg_{1-x}Cu_xV_2O_6$ series shows a change in structure from monoclinic brannerite ($C2/m$) to brannerite with a slight triclinic distortion ($P\bar{1}$) [17]. We can see the sample has a mixed phase starting from x = 0.4 with impurities. Based on the structural analysis (Figure 4a,b), the lattice parameters a, b, and c; angle β; and the unit cell volume are presented for the ranges x = 0.0–0.4 and x = 0.8–1.0. These variations are attributed to a miscibility gap between the $C2/m$ and $P\bar{1}$ space groups, leading to a mixture of phases with impurities at x = 0.6. The a and c parameters show a decrease in the lattice through the substitution of Mg^{2+} by Cu^{2+}, while the b parameters exhibit an increase. Since the ionic radii of Mg^{2+} and Cu^{2+} are 0.72 Å and 0.73 Å in the 6-fold coordination, respectively, as the copper content increases, the lattice parameters also exhibit a marginal increase [26]. The a and c parameters, however, show a decrease, and this probably can be explained by the structural distortion leading to lattice contraction. We can observe that the lattice parameter c exhibits a larger decrease compared to the other parameters. The change in the angle β and decrease in volume with the increasing amount of Cu^{2+} in the brannerite-type structure are observed in Figure 4c,d. Therefore, we can conclude that the shrinking of the brannerite structure, accompanied by distortion upon Cu^{2+} substitution, is influenced by the strong Jahn–Teller effect of Cu^{2+}.

In the series $Mg_{1-x}Co_xV_2O_6$ (x = 0.0–1.0) and $Mg_{1-x}Ni_xV_2O_6$ (x = 0.0–1.0), solid solutions were formed with some miscibility gaps. It is to be noted that CoV_2O_6 and NiV_2O_6 have a triclinic structure ($P\bar{1}$). These compounds were synthesized at 650 °C in air, and a phase transition was clearly observed in the series through XRD analysis, as shown in Figure S3. In the $Mg_{1-x}Co_xV_2O_6$ series, the phase transition to a triclinic structure ($P\bar{1}$) occurred when the cobalt content was x = 0.8. For compositions with $x \leq 0.6$, the major phase presented was a monoclinic structure ($C2/m$) with impurities. Similarly, in the series of $Mg_{1-x}Ni_xV_2O_6$ samples, the major phase of the brannerite structure was found for compositions $x \leq 0.1$, while for $x \geq 0.3$, compounds predominantly showed a triclinic

structure. Therefore, the presence of two distinct structures in the end members causes the series to exhibit a clear phase transition upon substitution.

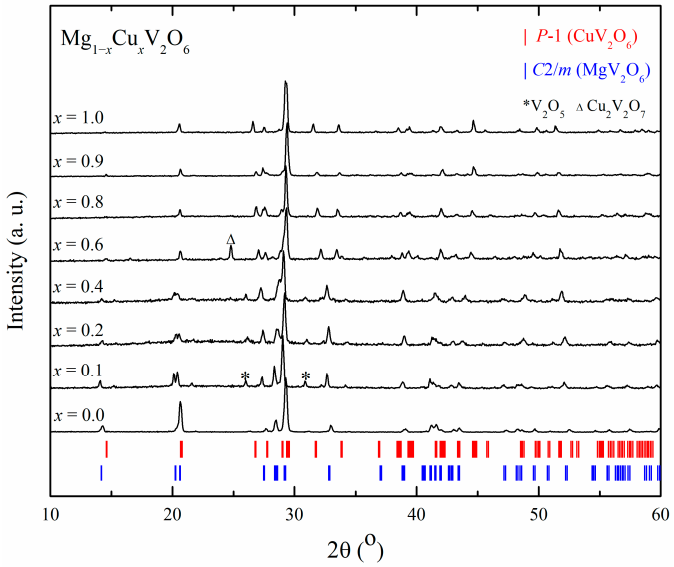

Figure 3. Powder XRD patterns of $Mg_{1-x}Cu_xV_2O_6$ (x = 0.0–1.0) samples prepared at 600 °C in air.

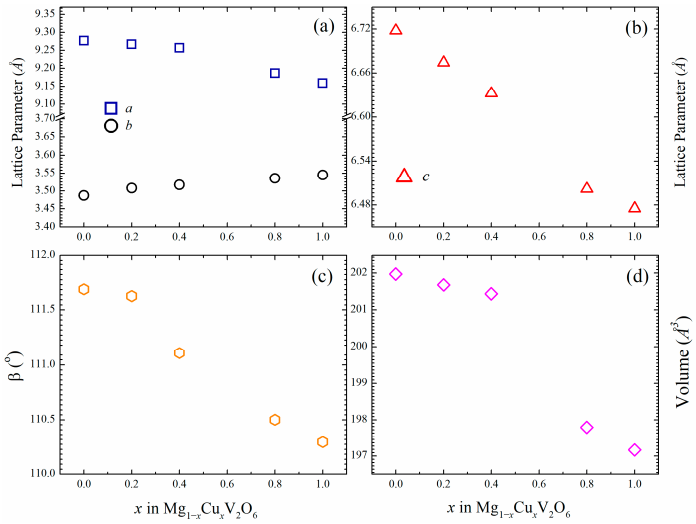

Figure 4. Variations in the (**a**) lattice parameters '*a*' and '*b*', (**b**) lattice parameter '*c*', (**c**) angle β, and (**d**) volume of the $Mg_{1-x}Cu_xV_2O_6$ series as a function of x.

The variations in the unit cell edges in the $Mg_{1-x}Co_xV_2O_6$ series show different scales in two regions: x = 0.0–0.6 and x = 0.8–1.0 (Figure S4). The lattice parameters do not change much except for '*c*', which shows a decrease with the increasing Co^{2+} composition from x = 0.0 to x = 0.6. It is possible that the Co^{2+} substitution leads to a decrease in the average distance between neighboring ions in unit cell *c*. For the triclinic structure (x = 0.8–1.0), the lattice parameters *a* and *c* increase as the cobalt content increases. This can be due to the larger ionic radius of Co^{2+} (0.735 Å) as compared to that of Mg^{2+} (0.72 Å) [26]. In the series of $Mg_{1-x}Ni_xV_2O_6$, with both end members having different structures (brannerite and NiV_2O_6 types), a decrease in the *a* and *c* lattice parameters was observed as the Ni^{2+} content increases (Figure S5). This can be attributed to the smaller ionic radius of Ni^{2+} (0.69 Å) when compared to Mg^{2+} (0.72 Å) [26]. The lattice parameter '*b*' also exhibits a decreasing trend upon the Ni^{2+} substitution in the NiV_2O_6 ($P\bar{1}$) phase ($x \geq 0.8$). Contrarily, the $C2/m$ phase ($x < 0.8$) shows an increase in the '*b*' lattice parameter when Ni increases.

To summarize, it is known that brannerite and NiV_2O_6-type structures have different segments within the morphotropic series and, hence, a miscibility gap between them.

3.2. Optical Properties

The samples in the $Mg_{1-x}M_xV_2O_6$ (*M* = Mn, Cu, Co, or Ni) series exhibit varying colors that can be understood by measuring the optical properties. The color of the $Mg_{1-x}Mn_xV_2O_6$ samples changes from brown to dark brown and eventually to black as the amount of Mn^{2+} increases (Figure S6a). The colors originate from the combination of band gap, d–d transitions, and charge transfers, transitions which can be confirmed by diffuse reflectance UV–Vis spectra of $Mg_{1-x}Mn_xV_2O_6$ samples, as shown in Figure S6b. The spectra show that, with the increasing concentration of Mn^{2+}, the optical absorption edges are red-shifted. This can be understood by narrowing of the band gap with the increasing Mn^{2+} concentration, as the end members of the solid solution MgV_2O_6 (E_g = 2.3 eV) and MnV_2O_6 (E_g = 1.44 eV) have different band gaps [17]. The band gap in these compounds can be considered as the difference in energy levels between the filled O 2p band and empty V 3d band. The absorption edges not only shift from 580 to 1000 nm but also show a variation in intensity, and these are evidence for the influence of Mn^{2+} on the ligand-to-metal charge transfer (LMCT: O^{2-}-V^{5+}) in $Mg_{1-x}Mn_xV_2O_6$. In addition to band gap (or LMCT) transition, the introduction of Mn^{2+} induces absorption bands in the visible region, as observed with humps in the region 450–550 nm for x = 0.1–0.7 and between 600 and 750 nm for x = 0.7. These absorptions are due to the d–d transition of Mn^{2+} in a distorted six-coordination environment. In general, Mn^{2+} in a perfect octahedral coordination with an inversion center does not exhibit any d–d transition [2]. However, the forbidden d–d transitions are enhanced in intensity because of the distorted octahedral coordination on Mn^{2+}. Also, the metal-to-metal charge transfer from half-filled Mn 3d orbitals to empty V 3d orbitals influences the color of the samples. The corresponding *L***a***b** color coordinates were calculated. The positive values of *a** indicate red hues, which decrease in the $Mg_{1-x}Mn_xV_2O_6$ series upon Mn^{2+} substitution. Similarly, the positive values of *b**, which represent yellow, decrease as well in this series. Furthermore, the lightness (*L**) decreases with the increase in the Mn^{2+} substitution, as listed in Table S1. The NIR reflectance spectra of the $Mg_{1-x}Mn_xV_2O_6$ samples are measured (Figure S6c). The percentage reflectance of $Mg_{1-x}Mn_xV_2O_6$ varies between 75% and 40% across the NIR region for x = 0.0 to x = 1.0, revealing a decrease in NIR reflectance with the increasing Mn^{2+}.

In the photographs of the samples, DRUV–Vis absorption and reflectance spectra of the $Mg_{1-x}Cu_xV_2O_6$ samples are shown in Figure 5. The DRUV–Vis reflectance spectrum of TiO_2 is also shown in Figure 5c (also in Figures S6–S8) as a comparison since it has a high NIR reflectance due to its high refractive index and application as a white, reflective pigment. In the UV–Vis spectra, it is clear that, as the amount of Cu^{2+} increases, the optical absorption edge is red-shifted from 600 to 780 nm, which can be understood as due to the decreasing band gap, which is different for MgV_2O_6 (E_g = 2.3 eV) and CuV_2O_6 (E_g = 1.69 eV) [16]. The broad optical absorption bands in the visible region (400–600 nm) indicate Cu 3d to V 3d metal–metal charge transfer (MMCT) transitions [27]. In the wavelength range of 650–900 nm, the weak absorption bands arise from partially filled Cu 3d e_g orbitals in the octahedral coordination. In addition, the $Mg_{1-x}Cu_xV_2O_6$ series with x = 0.2 to x = 1.0 exhibits a strong absorption in the near-IR region. The images of the samples and *L***a***b** parameters showing the color changes in the $Mg_{1-x}Cu_xV_2O_6$ series are presented in Figure 5a and Table 1, respectively. According to *L***a***b** color measurement, the solid-solution series $Mg_{1-x}Cu_xV_2O_6$ displays colors ranging from red to yellow hues, particularly the sample with x = 0.4, showing a more pronounced red hue. As

the concentration of Cu^{2+} increases, the color changes from yellowish to brown to black, which makes an agreement with the color measurement.

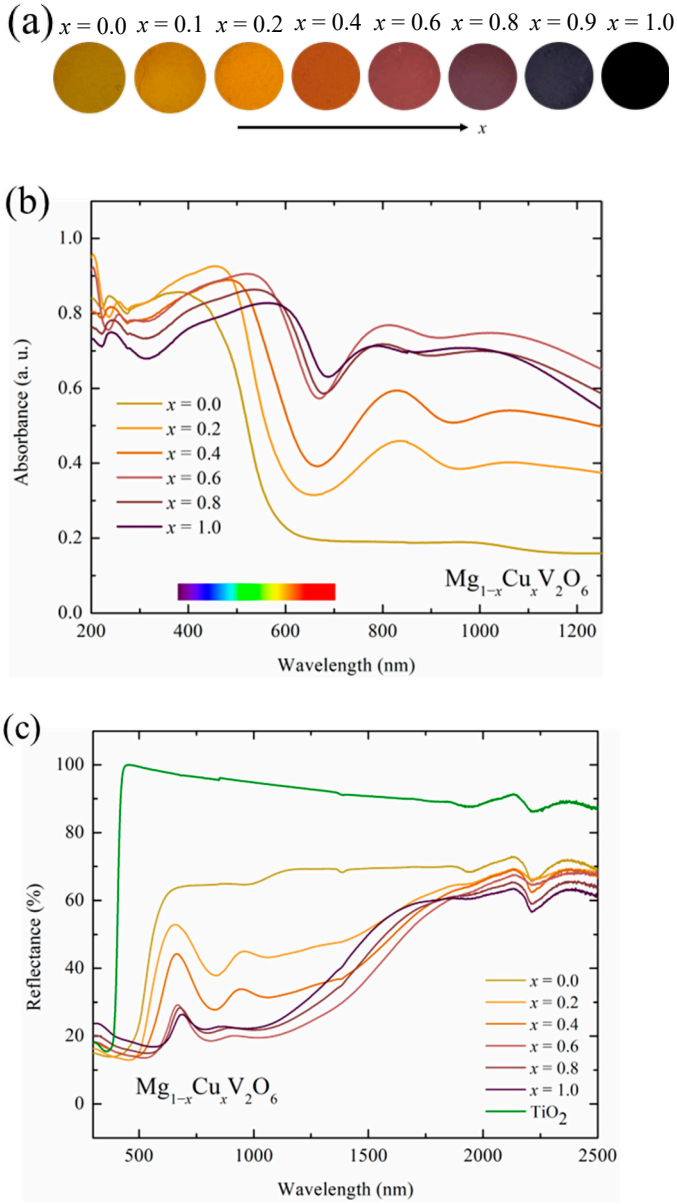

Figure 5. (**a**) Photographs, (**b**) DRUV–Vis absorbance, and (**c**) NIR reflectance spectra of $Mg_{1-x}Cu_xV_2O_6$ compounds. The NIR reflectance of TiO_2 is also shown for comparison in (**c**).

Table 1. The measured $L^*a^*b^*$ color coordinates of $Mg_{1-x}Cu_xV_2O_6$.

	L^*	a^*	b^*
$x = 0.0$	54.52	12.26	43.08
$x = 0.1$	45.23	16.20	32.47
$x = 0.2$	46.29	18.21	40.08
$x = 0.4$	36.18	20.79	21.89
$x = 0.6$	29.59	14.08	5.52
$x = 0.8$	28.29	8.43	2.42
$x = 0.9$	25.41	4.52	0.22
$x = 1.0$	21.61	3.88	0.08

In the series $Mg_{1-x}Co_xV_2O_6$, as in the previous cases, the color changes to dark, as shown in the photographs (Figure S7a), and the optical absorption edge shows a red

shift with the increasing Co^{2+} content (Figure S7b). Also, the compositions with x = 0.2, 0.4, and 0.6 show the distinct d–d transitions in the wavelength regions 650–780 nm and 780–1000 nm due to Co^{2+} present in the octahedral coordination environment. The variation in the optical absorption ($x < 0.8$ and $x \geq 0.8$) is attributed to the differences in the crystal structures (Brannerite vs. NiV_2O_6-type). This is similar to the observations of optical properties of Co^{2+} in $Zn_{1-x}Co_xV_2O_6$ with brannerite-type structures [17]. The NIR reflectance of the samples in the $Mg_{1-x}Co_xV_2O_6$ series exhibits a decrease from 70 to 20% with the increasing Co^{2+} concentration (Figure S7c). From the measured $L^*a^*b^*$ color coordinates for the $Mg_{1-x}Co_xV_2O_6$ samples, it is clear that the color shifts from yellowish to brown to dark brown and black as the cobalt composition increases (Table S2). For the sample with x = 0.4, the color has a more reddish tone as compared to the other compositions. Furthermore, it is evident that the yellow hue diminishes with the increasing cobalt content.

The color of the samples in the series $Mg_{1-x}Ni_xV_2O_6$ shows a change from brown to reddish brown to a dark color with the increasing Ni^{2+} concentration in Figure S8. The DRUV–Vis absorption spectra of these samples exhibit a red shift in the optical absorption edge with the increasing Ni^{2+}, and this is similar to the observed results with the introduction of transition metal ions in MgV_2O_6, as discussed above. The optical absorption occurs at 350 nm in the near-UV region due to the ligand–metal charge transfer (O^{2-} 2p → V^{5+} 3d). There are two absorption bands in the visible region located at ~ 450 nm and 750 nm, which indicate $^3A_{2g} \rightarrow {}^3T_{1g}$ (P) and $^3A_{2g} \rightarrow {}^3T_{1g}$ (F) transitions, respectively, of Ni^{2+} ions in the octahedral coordination [17,28]. In the NIR reflectance, the spectrum indeed shows an intense absorption from x = 0.2 to x = 1.0 and as the Ni^{2+} replacement increases, the percentage reflectance decreases. The $L^*a^*b^*$ color coordinates show a decreasing lightness (L^*), which means the samples become darker. Meanwhile, the b^* decreases, showing the decrease in yellow hue, and the composition with x = 0.5 has a more intense red color of a^* that is 20.23 (Table S3).

3.3. Magnetic Properties

To aid in understanding the microscopic origin of the color changes, the valence states of the transition metal ions can be deduced from the magnetic behavior of the compounds discussed above. It is known that MnV_2O_6 exhibits antiferromagnetic (AFM) behavior with non-frustrated Mn^{2+} ordering [29]. To understand the influence on the magnetic behavior upon the substitution of Mn^{2+} with Mg^{2+}, the magnetic properties of $Mg_{1-x}Mn_xV_2O_6$ (x = 0.9 and 1.0) were measured in the temperature range between 5 and 350 K, and the results are shown in Figure S9. It shows antiferromagnetic (AFM) ordering of Mn^{2+} in octahedral coordination, and the Néel temperatures (T_N) are 17.0 and 20.0 K, respectively. These values are in close agreement with the reported T_N of 20 K [29]. The results show that the decrease in T_N is consistent with the simple mean field dependence of the ordering temperature on the coordination number. Table 2 lists the calculated magnetic moments (μ_B), Curie constant, C (emu K/mol), and Weiss constant, Θ_{CW} (K). In order to prove the oxidation states of Mn in $Mg_{1-x}Mn_xV_2O_6$, we used the Curie–Weiss law to fit χ_{mol}^{-1} vs. T in the temperature range between 250 and 300 K, and from the linear region, the slope represents $1/C$ and y-intercept Θ_{CW}/C [29]. The negative values of Θ_W (Table 2) confirm the AFM nature of the nearest neighbor interaction, and the downturn in $1/\chi$ on cooling below 50 K indicates the likelihood of next-nearest-neighbor interactions. The calculated effective spin-only magnetic moments of the samples with x = 0.9 and 1.0 are 6.13 and 6.18 μ_B, respectively, and these values are in good agreement with the theoretical magnetic moment (5.92 μ_B) of the divalent Mn^{2+} ion. Thus, the oxidation state of manganese in $Mg_{1-x}Mn_xV_2O_6$ is confirmed as 2+.

Table 2. Observed magnetic moments μ_{eff} (μ_B), and Curie and Weiss constants of $Mg_{1-x}M_xV_2O_6$ (M = Mn, Cu, Co, and Ni). The theoretical spin-only magnetic moments are calculated for Mn^{2+} (d^5), Cu^{2+} (d^9), Co^{2+} (d^7), and Ni^{2+} (d^8).

Composition	Curie Constant (emu K/mol)	Weiss Constant (K)	Obs. Mag. Moment (μ_B)	Th. Mag. Moment (μ_B)
$Mg_{0.1}Mn_{0.9}V_2O_6$	4.69	−9.36	6.13	5.92
MnV_2O_6	4.77	−8.51	6.18	5.92
$Mg_{0.2}Cu_{0.8}V_2O_6$	0.58	−52.24	2.16	1.73
CuV_2O_6	0.57	−86.19	2.14	1.73
$Mg_{0.2}Co_{0.8}V_2O_6$	3.47	−12.22	5.27	3.87
CoV_2O_6	3.43	−11.35	5.24	3.87
$Mg_{0.1}Ni_{0.9}V_2O_6$	1.45	5.43	3.40	2.83
NiV_2O_6	1.42	6.80	3.37	2.83

For $Mg_{1-x}Cu_xV_2O_6$ (x = 0.8 and 1.0) in Figure 6, as the Cu concentration decreases, we observed a decrease in the magnetic ordering temperature. Additionally, at x = 1.0, antiferromagnetic ordering with T_N = 22 K is observed, consistent with previous studies [27]. In the inset in Figure 6, the molar susceptibility of CuV_2O_6 is displayed, and we observed that the magnitude of the ferromagnetic signal was around 3 emu/mol, which is very small compared to a FM saturation moment. This signal, which accounts for less than 0.1% of the compound, suggests the presence of uncompensated spins. We can conclude that the magnetic coupling is relatively weak in the structures. $Mg_{0.2}Cu_{0.8}V_2O_6$ exhibits magnetic interactions along the *b*-axis, with an edge-sharing octahedra contributing to ferromagnetic ordering. Based on the Curie–Weiss law in the temperature range between 250 and 300 K, a negative Curie temperature (Θ) suggests that the Cu^{2+} magnetic moments might overall exhibit antiferromagnetic correlations. The calculated effective moments for the samples with x = 0.8 and 1.0 are 2.16 and 2.14 μ_B, respectively (Table 2). The results show a slightly larger magnetic moment than the theoretical value (μ_{eff} = 1.73 μ_B); however, the values fall within the observed range and are consistent with the literature [27]. The enhanced effective magnetic moment is attributed to the partial orbital contribution resulting from Jahn–Teller distortion. This is further supported by the discussion of lattice parameters in the Structural Analysis (Section 3.1), with the structure of CuV_2O_6 shown in Figure 2a. The measurements confirm that the oxidation state of copper is indeed +2 in $Mg_{1-x}Cu_xV_2O_6$ (x = 0.8 and 1.0) within the structure.

Similarly, the samples of $Mg_{1-x}Co_xV_2O_6$ (x = 0.8 and 1.0) and $Mg_{1-x}Ni_xV_2O_6$ (x = 0.9 and 1.0) clearly exhibit antiferromagnetic ordering, as shown in Figures S10 and S11. When the concentrations of Co and Ni are decreased, these samples show a corresponding decrease in the ordering temperature. In the $Mg_{1-x}Co_xV_2O_6$ (x = 0.8 and 1.0) series, the AFM transition with Néel temperatures (T_N) was observed at 2.8 and 7.0 K, respectively, while the samples presented T_N at 14.5 and 15.0 K, respectively, in $Mg_{1-x}Ni_xV_2O_6$ (x = 0.9 and 1.0). It is worth noting that the susceptibility decreases by 10% in $Mg_{0.1}Ni_{0.9}V_2O_6$ compared to NiV_2O_6, which implies the sample was successfully synthesized as a solid solution. The observed magnetic moments in $Mg_{1-x}Co_xV_2O_6$ (x = 0.8 and 1.0) are 5.27 and 5.24 μ_B, respectively, which are much larger than the expected spin-only moment (3.87 μ_B) of high-spin Co^{2+} due to orbital contribution in the temperature range between 50 and 150 K. For the $Mg_{1-x}Ni_xV_2O_6$ (x = 0.9 and 1.0) samples, the observed magnetic moments of the Ni spins with S = 1 are 3.40 and 3.37 μ_B, respectively, in the temperature range between 50 and 200 K. According to the Curie–Weiss law results, the oxidation states of Co and Ni were confirmed as +2 in $Mg_{1-x}Co_xV_2O_6$ and $Mg_{1-x}Ni_xV_2O_6$.

Thus, the magnetic measurements of the studied brannerite samples helped in probing the oxidation states of the transition metal ions, which, in turn, explains the observed optical properties originating from d–d transitions, LMCT, and/or MMCT.

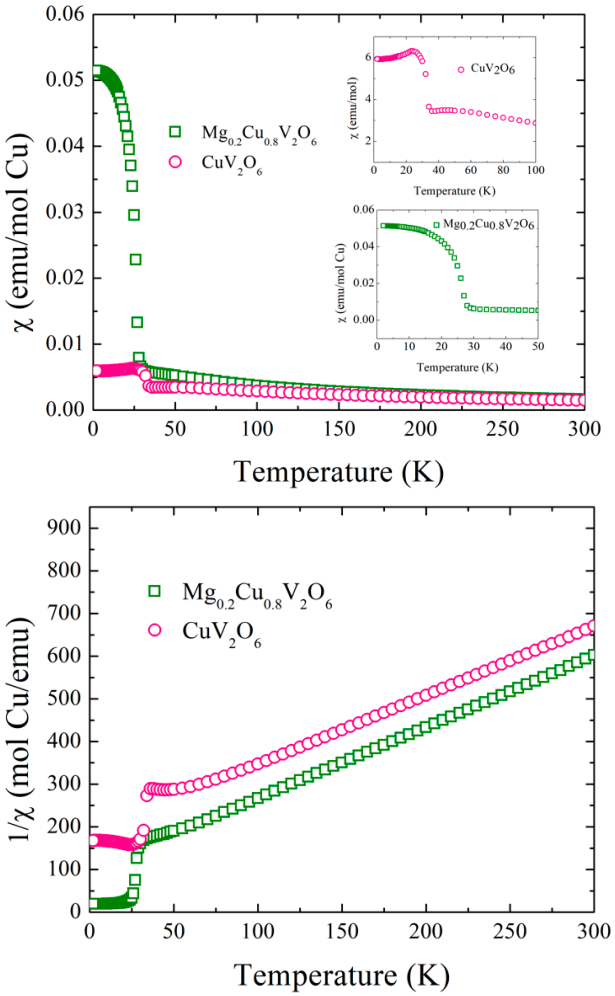

Figure 6. Magnetic susceptibility and inverse molar susceptibility vs. the temperatures of CuV_2O_6 and $Mg_{0.2}Cu_{0.8}V_2O_6$.

4. Conclusions

New brannerite-type solid solutions $Mg_{1-x}M_xV_2O_6$ (M = Mn, Cu, Co, or Ni) were synthesized, and their optical properties were studied. The results showed a miscibility gap between two segments of morphotropic transitions in solid solutions, causing phase transitions within the brannerite structure from $C2/m$ to $P\bar{1}$. The color and optical properties of these series originate from a combination of band gap, LMCT, MMCT, and d–d transitions. It was observed that $Mg_{1-x}Cu_xV_2O_6$ and $Mg_{1-x}Ni_xV_2O_6$ show more red hues in color with x = 0.4 and x = 0.5, respectively. Few compositions in the series $Mg_{1-x}Mn_xV_2O_6$ exhibit a high reflectance, which shows potential for their application as a 'cool' pigment. Furthermore, $Mg_{1-x}M_xV_2O_6$ (M = Mn, Cu, Co, or Ni) display antiferromagnetic behavior in the temperature range between 5 and 350 K. Further, the magnetic moments deduced from the measurements confirmed the presence of Mn^{2+}, Cu^{2+}, Co^{2+}, and Ni^{2+} in these series. It is worth exploring brannerite-type oxides as pigments due to their flexible compositional tuning with less expensive and non-toxic elements and relatively low temperature of synthesis.

Supplementary Materials: The following supporting information can be downloaded at https://www.mdpi.com/article/10.3390/cryst15010086/s1: Figure S1: Powder XRD patterns of $Mg_{1-x}Mn_xV_2O_6$ (x = 0.0–1.0) samples that were prepared at 700 °C in air; Table S1: The measured $L^*a^*b^*$ color coordinates of $Mg_{1-x}Mn_xV_2O_6$; Figure S2: Variations in the (a) lattice parameters 'a' and 'b', (b) lattice parameter 'c', (c) angle β, and (d) volume of the $Mg_{1-x}Mn_xV_2O_6$ series as a function of x; Table S2: The measured $L^*a^*b^*$ color coordinates of $Mg_{1-x}Co_xV_2O_6$; Figure S3: Powder XRD patterns of (a) $Mg_{1-x}Co_xV_2O_6$ and (b) $Mg_{1-x}Ni_xV_2O_6$ prepared at 650 °C in air; Table S3: The measured $L^*a^*b^*$ color coordinates of $Mg_{1-x}Ni_xV_2O_6$; Figure S4: Variations in the (a) lattice parameters 'a' and 'b' and (b) lattice parameter 'c' of the $Mg_{1-x}Co_xV_2O_6$ series as a function of x; Figure S5: Variations in the (a) lattice parameters 'a' and 'b' and (b) lattice parameter 'c' of the $Mg_{1-x}Ni_xV_2O_6$ series as a function of x; Figure S6: (a) Photographs, (b) DRUV–Vis absorbance, and (c) NIR reflectance spectra of the $Mg_{1-x}Mn_xV_2O_6$ solid solution series. The NIR reflectance of TiO_2 is also shown for comparison in (c); Figure S7: (a) Photographs, (b) DRUV–Vis absorbance, and (c) NIR reflectance spectra of the $Mg_{1-x}Co_xV_2O_6$ compounds, along with TiO_2; Figure S8: (a) Photographs, (b) DRUV–Vis absorbance, and (c) NIR reflectance spectra of the $Mg_{1-x}Ni_xV_2O_6$ compounds, along with TiO_2; Figure S9: Magnetic susceptibility and inverse molar susceptibility vs. the temperatures of MnV_2O_6 and $Mg_{0.1}Mn_{0.9}V_2O_6$; Figure S10: Magnetic susceptibility and inverse molar susceptibility vs. the temperatures of CoV_2O_6 and $Mg_{0.2}Co_{0.8}V_2O_6$; Figure S11: Magnetic susceptibility and inverse molar susceptibility vs. the temperatures of NiV_2O_6 and $Mg_{0.1}Ni_{0.9}V_2O_6$.

Author Contributions: N.L. conceived the research interest. H.-C.H. carried out the synthesis and properties characterization. A.P.R. conducted the magnetic measurements. M.A.S., N.L. and J.L. discussed the structural characterization and optical properties. All authors contributed to the drafting and editing of the manuscript. All authors have read and agreed to the published version of the manuscript.

Funding: The work done at Oregon State University was supported by NSF Grant No. DMR-2025615 (M.A.S.). The work done at UC Santa Cruz (A.P.R.) was supported by NSF Grant No. DMR-2218130.

Data Availability Statement: The research data will be made available on request.

Acknowledgments: The author N.L. acknowledges the United States–India Educational Foundation (USIEF) for the Fulbright-Nehru Academic and Professional Excellence Fellowship (2020–2021).

Conflicts of Interest: The authors declare no conflict of interest.

References

1. Subramanian, M.A.; Li, J. Challenges in the Rational Design of Intense Inorganic Pigments with Desired Colours. *Nat. Rev. Mater.* **2022**, *8*, 71–73. [CrossRef]
2. Subramanian, M.A.; Li, J. YInMn Blue—200 Years in the Making: New Intense Inorganic Pigments Based on Chromophores in Trigonal Bipyramidal Coordination. *Mater. Today Adv.* **2022**, *16*, 100323. [CrossRef]
3. Li, J.; Subramanian, M.A. Inorganic Pigments with Transition Metal Chromophores at Trigonal Bipyramidal Coordination: Y(In,Mn)O_3 Blues and Beyond. *J. Solid State Chem.* **2019**, *272*, 9–20. [CrossRef]
4. von Dreifus, D.; Pereira, R.; Rodrigues, A.D.; Pereira, E.C.; de Oliveira, A.J.A. Sol-Gel Synthesis of Triclinic CoV_2O_6 Polycrystals. *Ceram. Int.* **2018**, *44*, 19397–19401. [CrossRef]
5. Watanabe, M.; Muto, M.; Abe, Y.; Kaneko, T.; Toda, A.; Uematsu, K.; Ishigaki, T.; Sato, M.; Koide, J.; Toda, M.; et al. Synthesis of Red-Emissive CaV_2O_6 Nanophoshor via a Water Assisted Solid State Reaction Method. *ECS J. Solid State Sci. Technol.* **2021**, *10*, 106010. [CrossRef]
6. Wang, F.; Zhang, H.; Liu, L.; Shin, B.; Shan, F. Synthesis, Surface Properties and Optical Characteristics of CuV_2O_6 Nanofibers. *J. Alloys Compd.* **2016**, *672*, 229–237. [CrossRef]
7. Brannerite. Available online: https://www.sciencedirect.com/topics/earth-and-planetary-sciences/brannerite (accessed on 19 August 2023).
8. Beck, H.P. A Study on AB_2O_6 Compounds, Part III: Co-Ordination Needs and Patterns of Connectivity. *Z. Kristallogr. Cryst. Mater.* **2013**, *228*, 271–288. [CrossRef]
9. Ng, H.N.; Calvo, C. Crystal Structure of and Electron Spin Resonance of Mn^{2+} in MgV_2O_6. *Can. J. Chem.* **1972**, *50*, 3619–3624. [CrossRef]

10. Mocała, K.; Ziółkowski, J. Polymorphism of the Bivalent Metal Vanadates MeV_2O_6 (Me = Mg, Ca, Mn, Co, Ni, Cu, Zn, Cd). *J. Solid State Chem.* **1987**, *69*, 299–311. [CrossRef]
11. Jin, X.; Ding, X.; Qin, Z.; Li, Y.; Jiao, M.; Wang, R.; Yang, X.; Lv, X. Comprehensive Study of Electronic, Optical, and Thermophysical Properties of Metavanadates CaV_2O_6 and MgV_2O_6. *Inorg. Chem.* **2022**, *61*, 17623–17633. [CrossRef]
12. Kimber, S.A.; Mutka, H.; Chatterji, T.; Hofmann, T.; Paul, F.H.; Bordallo, H.N.; Argyriou, D.N.; Attfield, J.P. Metamagnetism and Soliton Excitations in the Modulated Ferromagnetic Ising Chain CoV_2O_6. *Phys. Rev. B* **2011**, *84*, 104425. [CrossRef]
13. Fernández de Luis, R.; Urtiaga, M.K.; Mesa, J.L.; Vidal, K.; Lezama, L.; Rojo, T.; Arriortua, M.I. Short-Range and Long-Range Magnetic Ordering, in Third Generation Brannerite Type Inorganic−Organic Vanadates: $[\{Mn(Bpy)\}(VO_3)_2] \approx (H_2O)_{1.16}$ and $[\{Mn(Bpy)_{0.5}\}(VO_3)_2] \approx (H_2O)_{0.62}$. *Chem. Mater.* **2010**, *22*, 5543–5553. [CrossRef]
14. Krasnenko, T.I.; Zabara, O.A.; Surat, L.L.; Strepetov, S.V. Investigation of the $Ca_{1-x}Mn_x(VO_3)_2$ Solid Solution. *Inorg. Mater.* **1987**, *23*, 1252–1254.
15. Hansen, S.; Nilsson, J.; Teixidor, F.; Viñas, C.; Abad, M.M.; Nielsen, R.I.; Olsen, C.E.; Rosendahl, C.N.; Haugg, M.; Trabesinger-Rüf, N.; et al. Coordination of Vanadium (5+) in Solid Solutions MgV_2O_6-CaV_2O_6 and ZnV_2O_6-CaV_2O_6. *Acta Chem. Scand.* **1996**, *50*, 512–515. [CrossRef]
16. Kozłowski, R.; Ziółkowski, J.; Mocała, K.; Haber, J. Defect Structures in the Brannerite-Type Vanadates. I. Preparation and Study of $Mn_{1-x}\phi xV_{2-2x}Mo_{2x}O_6$ ($0 \leq x \leq 0.45$). *J. Solid State Chem.* **1980**, *35*, 1–9. [CrossRef]
17. Lakshminarasimhan, N.; Li, J.; Hsu, H.-C.; Subramanian, M.A. Optical Properties of Brannerite-Type Vanadium Oxides, MV_2O_6 (M = Ca, Mg, Mn, Co, Ni, Cu, or Zn). *J. Solid State Chem.* **2022**, *312*, 123279. [CrossRef]
18. Calvo, C.; Manolescu, D. Refinement of the Structure of CuV_2O_6. *Acta Crystallogra. Sect. B Struct. Sci.* **1973**, *29*, 1743–1745. [CrossRef]
19. Prokofiev, A.V.; Kremer, R.K.; Assmus, W. Crystal Growth and Magnetic Properties of α-CuV_2O_6. *J. Cryst. Growth* **2001**, *231*, 498–505. [CrossRef]
20. Vasil'ev, A.N.; Ponomarenko, L.A.; Antipov, E.V.; Velikodny, Y.A.; Smirnov, A.I.; Isobe, M.; Ueda, Y. Short-Range and Long-Range Magnetic Ordering in α-CuV_2O_6. *Physica B* **2000**, *284–288*, 1615–1616. [CrossRef]
21. Müller-Buschbaum, H.K.; Kobel, M. Ein Neuer Strukturtyp Der Oxovanadate MV_2O_6: NiV_2O_6. *Z. Anorg. Allg. Chem.* **1991**, *596*, 23–28. [CrossRef]
22. Halcrow, M.A. Jahn–Teller Distortions in Transition Metal Compounds, and Their Importance in Functional Molecular and Inorganic Materials. *Chem. Soc. Rev.* **2013**, *42*, 1784–1795. [CrossRef]
23. Larson, A.C.; Dreele, R.B. *General Structure Analysis System*; Los Alamos National Laboratory Report; Los Alamos National Laboratory: Los Alamos, NM, USA, 2000; p. 86.
24. Toby, B.H. EXPGUI, a Graphical User Interface for GSAS. *J. Appl. Crystallogr.* **2001**, *34*, 210–213. [CrossRef]
25. Momma, K.; Izumi, F. *Vesta 3* for Three-Dimensional Visualization of Crystal, Volumetric and Morphology Data. *J. Appl. Crystallogr.* **2011**, *44*, 1272–1276. [CrossRef]
26. Shannon, R.D. Revised Effective Ionic Radii and Systematic Studies of Interatomic Distances in Halides and Chalcogenides. *Acta Crystallogr. Sect. A* **1976**, *32*, 751–767. [CrossRef]
27. Hossain, M.K.; Sarker, H.P.; Sotelo, P.; Dang, U.; Rodríguez-Gutiérrez, I.; Blawat, J.; Vali, A.; Xie, W.; Oskam, G.; Huda, M.N.; et al. Phase-Pure Copper Vanadate (α-CuV_2O_6): Solution Combustion Synthesis and Characterization. *Chem. Mater.* **2020**, *32*, 6247–6255. [CrossRef]
28. Rossman, G.R.; Shannon, R.D.; Waring, R.K. Origin of the Yellow Color of Complex Nickel Oxides. *J. Solid State Chem.* **1981**, *39*, 277. [CrossRef]
29. Kimber, S.A.; Attfield, J.P. Disrupted Antiferromagnetism in the Brannerite MnV_2O_6. *Phys. Rev. B* **2007**, *75*, 064406. [CrossRef]